3D sub-cellular localization of upconverting nanoparticles through hyperspectral microscopy

Rodolfo N. Silva[a, b], Alexandre M. P. Botas[a], David Brandão[c], Verónica Bastos[c], Helena Oliveira[c], Mengistie L. Debasu[a], Rute A. S. Ferreira[a], Carlos D. S. Brites[a*], Luís D. Carlos[a*]

[a] Phantom-g, CICECO – Aveiro Institute of Materials, Department of Physics, University of Aveiro, 3810–193 Aveiro, Portugal
[b] Departamento de Química Fundamental, Universidade Federal de Pernambuco, 50740-540, Recife, PE, Brazil
[c] CESAM – Centre for Environmental and Marine Studies, University of Aveiro, 3810–193 Aveiro, Portugal

Abstract

Hyperspectral microscopy is an intriguing technique combining spectroscopy with optical microscopy that can be used to simultaneously obtain spectral and spatial information. The relevance of hyperspectral imaging in biomedical applications such as the monitoring of bioimaging agents, the identification of pathogens and cancerous cells, and the cellular uptake of nanoparticles has emerged recently, due to recent advances in optical reconstruction. The location and tracking of particles within the cell structure have been analyzed by 2D hyperspectral imaging of non-fluorescence objects, being examples of 3D localization uncommon. Here, we report the synthesis of Yb^{3+}/Er^{3+}-codoped Gd_2O_3 nanoparticles, their structural and luminescence characterization, and their biocompatibility assessments in Human melanoma (MNT-1 and A375) cell lines. The internalization of the particles by MNT-1 cells and their 3D localization in a fixed configuration are addressed through 2D optical images acquired in different planes along with the cell culture depth. 2D hyperspectral imaging is used to unequivocally identify the nuclei and the nanoparticles. The results indicate that the particles are distributed in distinct planes deep in the cell volume in the cytoplasmic and perinuclear regions. Furthermore, the emission signature of the nanoparticles enabled the determination of the intracellular temperature.

Keywords: Hyperspectral Microscopy; 3D Localization, Trivalent Lanthanide Ions, Upconversion, Nanoparticles, Cellular Uptake.

1. Introduction

Hyperspectral microscopy is a well-known technique combining imaging and spectroscopy [1, 2]. The technique generates a three-dimensional (3D) dataset of spatial and spectral information, known as hypercube, by collecting spectral information at each pixel of a two-dimensional (2D) detector array [3, 4]. Originated from remote sensing [1], hyperspectral imaging has been found, however, applications in other areas, such as food quality control [5, 6], safety [6], and materials science [7]. Due to recent advances in optical re-construction, hyperspectral images combined with optical microscopy emerged in recent years as a promising and powerful optical technology for biomedical applications [3, 8], namely for spatial-scanning analysis of single-cell and complex biological systems [9-11]. For instance, spatially resolved spectral imaging provided diagnostic information about tissue physiology, morphology, composition [3], and metabolic activity [8, 12]. Moreover, as the method is sensitive to subtle spectral changes it can be used to discriminate chemical or biological entities,[11] to localize and track nanoparticles in cells [7, 10, 13-21], or to identify pathogens and cancer cells [3, 22-25].

In the great majority of the examples reported so far, the cellular uptake of nanoparticles, and their location and tracking within the cell structure, was studied through 2D hyperspectral images of non-fluorescence objects. Exceptions concerning 3D imaging are the mappings of Ag and CeO_2 nanoparticles internalized in cells of the green alga [26], CD44-targeted PEGylated Au nanoparticles in fixed cell preparations [27], Ag and Au nanoparticles labeling live-cell organelles [28], and the transmembrane process of cell-penetrating peptide modified Au nanoparticles[29]. There are no reports of 3D imaging of luminescent nanoparticles; as far as we know, there are only examples of detection of fluorescent dyes at depth in tissue-mimicking phantoms [30].

Here we report the synthesis of Yb^{3+}/Er^{3+}-codoped Gd_2O_3 nanoparticles (as an illustrative example), their structural characterization, photoluminescence features, and their cytotoxicity assessments in Human melanoma MNT-1 and A375 cell lines. To discuss the internalization of the particles by MNT-1 cells and their 3D localization, 2D optical images are acquired in different planes along with the cell culture depth. Hyperspectral images of the same areas permit the unequivocal identification of the nuclei of the cells and nanoparticles. The incubated Yb^{3+}/Er^{3+}-codoped Gd_2O_3 nanoparticles particles are distributed in the cytoplasmic and perinuclear regions of the fixed MNT-1 cells in distinct planes deep in the cell volume. Moreover, as an added benefit, the emission fingerprint of the internalized nanoparticles enables the determination of the MNT-1 intracellular temperature.

2. Experimental

2.1. Synthesis

$(Gd,Yb,Er)_2O_3$ nanoparticles: Spherical $(Gd,Yb,Er)_2O_3$ nanoparticles were synthesized following a procedure [17] modified from a previously established methodology [31]. In a typical procedure, aqueous solutions of $Gd(NO_3)_3$ (2.94 mL, 0.4 M), $Yb(NO_3)_3$ (0.030 mL, 0.4 M), and $Er(NO_3)_3$ (0.120 mL, 0.1 M) were mixed in distilled water (200 mL). Urea (2.7 g) and hexadecyltrimethylammonium bromide (CTAB) (0.6 g) were dissolved in this solution under ultrasonication and magnetic stirring. The mixture was heated up at 358 K and the reaction was refluxed for 3 h. The final product was washed with distilled water and ethanol several times, collected *via* centrifugation (600 rpm, 25 min),

and dried at 348 K for 24 h. To obtain crystalline $(Gd_{0.97}Yb_{0.02}Er_{0.01})_2O_3$ nanoparticles (where the concentrations are the nominal molar concentrations) the dried powder was calcined at 1073 K for 3 h.

2.2. Methods

Powder X-ray diffraction: Diffraction patterns were collected on a powder X-ray diffractometer (PANalytical Empyrean) using Cu-$K_{\alpha 1}$ radiation (0.1540 nm, 45 kV, 40 mA) in the reflection spinning scan mode in the range 15.00 – 50.00° (2θ) with a 0.04 degrees step and 1.8 s acquisition time per step.

Electronic microscopy: The morphology of the samples was analyzed on a Hitachi H9000 transmission electron microscope (TEM) operated at 200 kV.

Photoluminescence: The upconversion emission spectra were recorded at room temperature on a Fluorolog®-3 Horiba Scientific (Model FL3-2T) spectroscopy, with a TRIAX 320 single-emission monochromator (fitted with a 1200 grooves mm^{-1} grating blazed at 500 nm, reciprocal linear density of 2.6 nm mm^{-1}), coupled to an R928 Hamamatsu photomultiplier, using the lateral face acquisition mode. The excitation source was a 980 nm continuous wave laser diode (Thorlabs LDM21 mount, LDC220 laser diode controller, and TED200 temperature controller) focused using a C230TM-B aspheric lens (Thorlabs). The emission spectra were corrected for the detection and optical spectral response of the spectrofluorometer using a photodiode reference. The laser power on the sample was measured using a FieldMaxII-TOP Laser Power and Energy Meter (Coherent Inc.) coupled with a neutral density filter (NE10B-B, Thorlabs) to avoid saturation of the power meter at high laser power. The average diameter of the spot area on the sample is 406 µm.

Cell lines and culture conditions. Human melanoma MNT-1 cells were kindly provided by Manuela Gaspar (iMed.ULisboa, Portugal). A375 cell line was purchased from the European Collection of Authenticated Cell Cultures (ECACC) and supplied by Sigma-Aldrich (Spain). MNT-1 and A375 cells were aseptically grown in Dulbecco's modified Eagle's medium (DMEM), supplemented with 10% FBS, 2 mM l-glutamine, 100 U/mL penicillin–100 µg·mL^{-1} streptomycin, and 2.5 µg·mL^{-1} fungizone in a humidified incubator at 310 K and 5% CO_2.

Viability assessment. The effect of the nanoparticles on cell viability was determined by the colorimetric MTT assay, which measures the formation of purple formazan in viable cells [32]. MNT-1 and A375 cells were seeded in 96 wells plates with four technical replicates in each assay of 24 h and 48 h. MNT-1 were seeded at 3500 and 2000 cells per well for 24 and 48 h exposure, respectively, while A375 were seeded at 3500 and 2500 cells per well for 24 and 48 h exposure, respectively. After adhesion, cells were incubated for 24 and 48 h with $(Gd_{0.97}Yb_{0.02}Er_{0.01})_2O_3$ nanoparticles at 0, 12.5, 25, 50, 100, and 200 µg·mL^{-1}. Control cells were incubated with a culture medium. At the end of the incubation time, the wells were emptied, washed with the phosphate-buffered saline (PBS) solution to remove the remaining particles, and a fresh medium (100 µL) was placed in each well. After that, 50 µL of MTT (1 mg. mL^{-1} in PBS) was added to each well and incubated for 4 h at 310 K in a 5% CO_2 humidified atmosphere. Thereafter, the culture medium with MTT was removed and replaced by 150 µL of DMSO to dissolve the formazan crystals. The absorbance was measured with a plate reader

(Synergy HT Multi-Mode, BioTeK, Winooski, VT) at 570 nm with blank corrections. The cell viability (*V*) was calculated, with respect to the control cells, using:

$$V\ (\%) = \frac{A_s - A_{DMSO}}{A_c - A_{DMSO}} \times 100\%, \qquad \textbf{(1)}$$

where A_s, A_{DMSO} and A_c stand for the absorbance values of the sample, DMSO, and control, respectively.

Microscopy sample preparation. MNT-1 cells were grown on glass coverslips and cultured in the presence of the $(Gd_{0.97}Yb_{0.02}Er_{0.01})_2O_3$ nanoparticles at 25 and 100 µg·mL^{-1} dispersed in culture medium, for 24 h. After that, cells were fixed with 4% paraformaldehyde in PBS for 10 min. Following washes with PBS and deionized water, coverslips were mounted onto glass slides with 4',6-diamidino-2-phenylindole (DAPI)-containing Vectashield mounting medium (Vector Labs).

Optical Microscopy. The optical microscopy images were recorded using an Olympus BX51 microscope (50× and 100× objectives), equipped with a color (Retiga 4000R, QImaging) and a monochrome (01-QI825-M-16-C, QImaging) digital CCD cameras. The bright-field images (in transmission and reflection modes) were acquired under white light (DC regulated illuminator, DC-950, Fiber-Lite), UV (LED light, LLS-365, Ocean Optics, emission at 365 ± 25 nm), or NIR (CW 980 nm laser diode, PSU-H-LED, CNI Lasers) irradiations. A scheme of the setup is presented in Figure 1a. The laser power density (0.25 ± 0.02 W.cm^{-2}) is homogeneous in the analyzed area, as previously reported [33] (Figure S1 in Supporting Information).

Hyperspectral Microscopy: The hyperspectral microscope images were performed with a digital camera (IPX-2M30, Imperx) coupled to a spectrograph (V10E 2/3", Specim, 30 µm slit, nominal spectral range of 400–1000 nm, and nominal spectral resolution of 2.73 nm). Each pixel field-of-view of the hyperspectral images recording with the 100× objective corresponds to 129×129 nm^2, on the plane of the samples. The hyperspectral scanning is performed line-by-line, with a total of 696 lines using an exposure time of 3.0 s per line. All the hyperspectral data were acquired and analyzed using the ®ENVI 4.8 software.

3D imaging system. The 3D images were created using the custom CytoViva Acquisition Software by acquiring 320 optical microscopy images (2D optical sections), with the monochrome digital CCD camera, at different surface depths using an automatic piezo-driven *z*-axis stage (Nano-Z Series, Mad City Labs) and a distance between optical sections (Δ*z*) of 200 nm (Figure 1b,c). For the nuclei of the cells, the 2D optical sections were recorded in bright field reflection mode under UV irradiation. The images were obtained by deconvolution assuming that the optical path through the instrument is optically perfect, and convoluted with a point spread function (PSF), *i.e.*, a mathematical function describing the distortion of the optical path by a point source of light through the instrument. The used PSF is based on the numerical aperture and index of refraction of the objective, the index of refraction of the media, and the DAPI emission wavelength. For the nanoparticles, the 2D optical sections were recorded in dark-field transmission mode using the CytoViva enhanced dark-field illumination system (CytoViva, Auburn, AL, USA), under red light illumination. The irradiation band (552-592 nm, peak at ~580 nm) was achieved by filtering the white light from the illuminator (Lumen 200, Prior) by a dual-mode fluorescence module. The location of the nanoparticles uses their

scattering intensity since the regions where the nanoparticles are located are those presenting higher scattering intensity (Figure S3). The positions of the particles are detected searching along each column of pixels - that result from the stacking of the images acquired along the z dimension - the localization of the object with the highest scattering intensity. The pixel with the highest intensity is considered as the location of the center of the nanoparticle and is represented in the 3D image by a sphere. Only the pixels with intensity above a certain threshold were considered to eliminate the contribution of the background signal.

Statistical analysis of cellular viability. The statistical significance of disparities between control and exposed cells was evaluated by one-way ANOVA, followed by Dunnett's test using the Sigma Plot 12.5 software (Systat Software Inc.). A value of $p<0.05$ was considered statistically significant.

3. Results and Discussion

3.1. Structural characterization

Figure 2a,b shows TEM micrographs of the calcined $(Gd_{0.97}Yb_{0.02}Er_{0.01})_2O_3$ nanoparticles displaying uniform spherical morphology with a particle size of 60 ± 4 nm and a typical rougher surface. The nanoparticles present a diffraction pattern compatible with that of the undoped Gd_2O_3 cubic phase reference (Figure 2c). Moreover, in Figure 2b the distance between adjacent lattice fringes, 0.312 ± 0.002 nm, matches the respective d_{222} value (0.31 nm) of the cubic Gd_2O_3 structure (JCPDS No. 04-003-4699). The uncertainty of the lattice fringes was obtained using the standard deviation from the lattice fringes distance distribution.

The $(Gd_{0.97}Yb_{0.02}Er_{0.01})_2O_3$ nanoparticles are moderately dispersible in water presenting a zeta-potential of 10 ± 4 mV and a hydrodynamic size distribution cantered at 156 ± 52 nm (Figure S2 in Supporting Information).

When NPs are delivered into cell culture media, their colloidal and chemical properties can be altered due to the presence of proteins and the high ion content. Several reports (*e.g.*, J. Mater. Chem., 2010,20, 6176-6181; J. Mater. Chem., 2010,20, 512-518; Materials 2021, 14, 1657) have demonstrated that serum proteins at a typical concentration of 10% can improve the colloidal stability due to extra electrosteric repulsion provided by proteins adsorbed on the particle surface. Therefore, we expect that serum proteins present in culture medium may have increased the stability of $(Gd_{0.97}Yb_{0.02}Er_{0.01})_2O_3$ nanoparticles resulting in the formation of smaller agglomerates.

3.2. Upconversion emission

The emission spectra of the $(Gd_{0.97}Yb_{0.02}Er_{0.01})_2O_3$ nanoparticles display the characteristic $^2H_{11/2}\rightarrow{}^4I_{15/2}$ and $^4S_{3/2}\rightarrow{}^4I_{15/2}$ transitions (in the green spectral region, Figure 3a, and the $^4F_{9/2}\rightarrow{}^4I_{15/2}$ line (in the red spectral region, not shown). The dependence of the emission spectra with the laser power density (P_D) shows a relative decrease of the $^4S_{3/2}\rightarrow{}^4I_{15/2}$ transition as P_D increases, a clear sign of temperature augmentation induced by the 980 nm laser irradiation [34, 35]. This is evident in Figure 3b that displays the P_D dependence of the ratio between the integrated intensities of the

$^2H_{11/2} \rightarrow {}^4I_{15/2}$ (I_H) and $^4S_{3/2} \rightarrow {}^4I_{15/2}$ (I_S) transitions, define as the so-called thermometric parameter $\Delta = I_H/I_S$.

3.3. Cell viability

Figure 4 shows the *in vitro* cell viability of MNT-1 and A375 melanoma cells treated with $(Gd_{0.97}Yb_{0.02}Er_{0.01})_2O_3$ nanoparticles for 24 and 48 h. The nanoparticles decreased the viability of MNT-1 cells only at the concentration of 200 $\mu g \cdot mL^{-1}$. For exposure periods of 24 and 48 h the cell viability above the 70% threshold (according to the norm ISO 10993-5:20099(en) [43]) is similar, 82.4±1.2 % and 86.6±11.2 %, respectively. Regarding the effects on A375 cells, the nanoparticles did not affect the cell viability at 24 h but induced a decrease in cell viability for the highest concentrations (87.7±## % for 100 $\mu g \cdot mL^{-1}$ and 82.5±## %% for 200 $\mu g \cdot mL^{-1}$) after 48 h. Nevertheless, the viability of both cell lines is above the 70% threshold [43] and the $(Gd_{0.97}Yb_{0.02}Er_{0.01})_2O_3$ nanoparticles can be considered non-cytotoxic, at the range of tested concentrations. These results concur with our previous study with the exposure of $(Gd_{0.98}Nd_{0.02})_2O_3$ nanoparticles to MNT-1 cells, which did not induce toxicity by 24 h exposure for concentrations up to 400 $\mu g \cdot mL^{-1}$ [44].

3.4. Hyperspectral microscopy and 3D localization

Figure 5a displays a bright-field optical image of DAPI-marked MNT-1 cells exposed to $(Gd_{0.97}Yb_{0.02}Er_{0.01})_2O_3$ nanoparticles in a fixed cell preparation. Nanoparticles clusters of different sizes and degrees of aggregation are visible as dark spots and the nuclei delimitations were detected under UV light illumination by the DAPI staining (fluorescence in the blue spectral range, peaking at 460 nm), Figure 5b, showing overlaid cells due to the density used during the culturing process.

The blue rectangle shown in Figure 5 is magnified in Figure 6a corresponding to the selected area to study the internalization and localization of the Yb^{3+}/Er^{3+}-codoped Gd_3O_2 nanoparticles combining 2D optical and hyperspectral images. Under 980 nm irradiation, the optical images of the DAPI-marked MNT-1 cells treated with $(Gd_{0.97}Yb_{0.02}Er_{0.01})_2O_3$ nanoparticles reveal bright spots with distinct intensities displaying red (clusters II and IV) and yellow (clusters I and III) colors, Figure 6b. As the biological medium has very low absorption at 980 nm, cell autofluorescence is negligible improving, thus, the detection of the upconverting emission. The emission spectra recorded in the hyperspectral image of Figure 6c, (that corresponds to the same region depicted in Figure 6a,b), display the $^2H_{11/2} \rightarrow {}^4I_{15/2}$ and $^4S_{3/2} \rightarrow {}^4I_{15/2}$ transitions, Figure 6d, demonstrating unequivocally that the bright spots correspond to $(Gd_{0.97}Yb_{0.02}Er_{0.01})_2O_3$ clustering.

The emission spectra shown in Figure 6d also point out that the distinct colors of the bright spots in Figure 6b are due to distinct intensity ratios between the emissions in the green ($^2H_{11/2} \rightarrow {}^4I_{15/2}$/$^4S_{3/2} \rightarrow {}^4I_{15/2}$) and red ($^4F_{9/2} \rightarrow {}^4I_{15/2}$) spectral regions. The spatial variation of the red-to-green (R/G) intensity ratio has already been reported for confocal [45] and hyperspectral [7] microscopy imaging of single Yb^{3+}/Er^{3+}-codoped $LiYF_4$ microparticles. In the first example, the R/G intensity ratio varies twofold depending on if the collected emission arises from the apex, an arris, or a face of the single microcrystals [45], while in the other work the variation (also twofold) is linked to

the spatial microparticle orientation (difference in the probed emission direction relative to the optic axes of the particles) [7]. Furthermore, the R/G intensity ratio is also dependent on the collection area in the hyperspectral images, as shown in Figure S4 in Supporting Information for region IV. This was also reported for β-$NaYF_4$:Yb^{3+}/Er^{3+} nanoparticles dispersed in polydimethylsiloxane-based organic-inorganic hybrids [46] and Yb^{3+}/Er^{3+}-codoped GeO_2-Ta_2O_5 particles dispersed in poly(methyl methacrylate) [33].

Heterogeneous Yb^{3+}/Er^{3+} dopant distribution, a difference in the crystal field strength experienced by dopant ions occupying different crystallographic sites within the lattice of the particle, uneven surface-ligand coverage[7], and distinct surface/volume ratios of the particles (or corresponding clusters) [33, 46], have been all suggested as tentative explanations for the observed R/G intensity ratio variation. Although for the uniaxially birefringent crystalline $LiYF_4$ host, single-particle polarized emission spectroscopy confirmed that the spatial emission intensity variation exhibited during hyperspectral imaging is due to direction-dependent polarized emission [7], for other examples (as the one reported here) a comprehensive explanation is still needed.

In what follows, we use the 3D location of the nanoparticles in Figure 6c to explain their different brightness. The creation of the 3D image with the representation of the location of nanoparticles requires the ability to collect a signature signal [10]. Here, we used the scattering of the $(Gd_{0.97}Yb_{0.02}Er_{0.01})_2O_3$ nanoparticles as the signature signal because is a well-established method for the detection and location of nanoparticles, especially when using the CytoViva enhanced dark-field illumination system [10, 20, 26, 47], as it is the case here. Moreover, although the upconversion emission signal can also be used as an alternative signature signal, as, for example, reported in reference [7], the hyperspectral images of Figure S3 in Supporting Information show that the pixels where the emission of the nanoparticles is detected correspond exactly to those pixels where the scattering intensity is higher.

Figure 6e shows a 3D image with the colocalization of the nuclei of the cells and nanoparticles. The image was created by overlay one 3D image of the cell nuclei and one 3D image representing the localization of the nanoparticles. Each 3D image was obtained by processing sets of optical microscopy images obtained along the spatial dimension *z*. The image of the nuclei of the cells was obtained from the deconvoluted images recorded under UV irradiation. Deconvolution is the process of reversing the optical distortion that takes place in an optical microscope to create clear images [48]. The image with the representation of the position of the nanoparticles was obtained by analyzing the scattering signal observed in the optical images in dark field mode. 3D images show clearly that the $(Gd_{0.97}Yb_{0.02}Er_{0.01})_2O_3$ nanoparticles are distributed in a distinct plane deep in the cell volume in the cytoplasmic and perinuclear regions. This result undoubtedly proves the cell internalization of the nanoparticles. The fact that the clusters of the nanoparticles are in different planes along the *z*-axis (Figure 6e) explains the differences in the brightness of the distinct clusters observed in Figure 6b. It is the case of clusters II and III that are located in a plane closer to the top surface of the cell culture, at $z \approx 9$ μm, their emissions are brighter than that of cluster IV that corresponds to particles located much deeper within the analyzed cell culture volume at $z \approx -8$ μm. The fact that the clusters are positioned at distinct *z* coordinates means that when we obtain a single 2D optical image, like the one in Figure 6b, we are getting emission signals from clusters of nanoparticles located at distinct *z* coordinates and, thus, at distinct distances from the focal plane of the objective. Clusters of nanoparticles located at a larger distance of the focal plane of the objective

will appear in the 2D optical image with less intensity (*i.e.*, less brightness). The size and the shape of the clusters also impact their brightness on the 2D optical images. For example, if two clusters are situated at the same *z* plane but with distinct sizes, the larger one presents higher intensity (since it has more nanoparticles at/near the focal plane). The collection of several 2D images along with the *z*-axis, *i.e.* by moving the phocal plane of the objective along the *z*-axis, allows the creation of a 3D image that can give information not only about the spatial position of the clusters along with the *z*-axis but also about the shape and size of the clusters, as shown in Figure 6e.

Finally, using the concept of primary thermometers applied to the thermally-coupled $^2H_{11/2}$ and $^4S_{3/2}$ Er^{3+} electronic levels, introduced by some of us in 2017, we can write the absolute temperature (*T*) as [49]:

$$\frac{1}{T} = \frac{1}{T_0} - \frac{k_B}{\Delta E}\ln\left(\frac{\Delta}{\Delta_0}\right), \qquad \textbf{(2)}$$

where T_0 is the room temperature, ΔE is the energetic separation between the barycenters of the $^2H_{11/2}$ and $^4S_{3/2}$ levels, k_B is the Boltzmann constant, and Δ_0 is the value of Δ at T_0. This innovative concept to predict the temperature does not require a conventional calibration procedure and is used in what follows to determine the temperature of the culture medium imaged in Figure 5 and Figure 6. Considering Δ_0 = 0.28 ± 0.01 (Figure 3b), ΔE = 762 cm^{-1} [17], T_0 = 298 ± 1 K (the temperature in the microscope room), and the Δ values calculated from the emission spectra recorded by the hyperspectral system in regions I (0.28 ± 0.01) and II (0.28 ± 0.02), Figure 6a-c, the absolute temperature calculated from Eq. 2 is 298 ± 1 and 298 ± 2 K, for regions I and II, respectively. Whereas the uncertainty in the Δ values are calculated accordingly to Eq. S3 in Supporting Information, error propagation in Eq. 2 yields the temperature uncertainty.

As expected, these values match the registered room temperature since the cells under observation are in a fixed configuration. Moreover, the agreement between the temperature values calculated for the two regions confirms that despite their distinct R/G intensity ratios there are no temperature gradients within the cell culture, as it is obviously expected for fixed cells [50, 51].

4. Conclusion

$(Gd_{0.97}Yb_{0.02}Er_{0.01})_2O_3$ nanoparticles were prepared with uniform spherical morphology, displaying an average size of 60 ± 4 nm, a typical rougher surface, and moderately dispersibility in water. Their emission spectra under 980 nm excitation present the characteristic $^2H_{11/2}\rightarrow{}^4I_{15/2}$, $^4S_{3/2}\rightarrow{}^4I_{15/2}$, and $^4F_{9/2}\rightarrow{}^4I_{15/2}$ Er^{3+} transitions whose intensity depends on the laser power density and temperature. In particular, the dependence of the ratio between the integrated intensities of the former two lines on the temperature, the so-called thermometric parameter $\Delta = I_H/I_S$.

The $(Gd_{0.97}Yb_{0.02}Er_{0.01})_2O_3$ nanoparticles showed no cytotoxicity (at the range of concentrations tested) to the melanoma MNT-1 and A375 cell lines and were successfully internalized by the former cells. The 3D sub-cellular localization of the nanoparticles in MNT-1 cells in a fixed configuration was

achieved processing sets of optical microscopy images obtained along with the spatial dimension *z*. The corresponding 2D hyperspectral images are used to unequivocally identify the nuclei and the nanoparticles. The results pinpoint the upconverting nanoparticles relatively to the nuclei of the cells distributed in distinct planes deep in the cell volume in the cytoplasmic and perinuclear regions. As a proof-of-concept experiment, the intracellular temperature was calculated using the emission spectra recorded at fixed cells, recovering a temperature value that is compatible with the room temperature. As far as we know, this is the first time that this strategy is applied to luminescent nanoparticles and can be used in real-time providing new avenues in the spatio-temporal characterization and detection of bio-analytes.

Acknowledgments

The work was partially developed under the project CICECO – Aveiro Institute of Materials, UIDB/50011/2020 & UIDP/50011/2020, and CESAM, UIDP/50017/2020 & UIDB/50017/2020, UID/QUI/00062/2019, financed by Portuguese funds through the FCT/MEC and when appropriate co-financed by FEDER under the PT2020 Partnership Agreement. Financial support from the projects NanoTBTech (European Union's Horizon 2020 FET Open program under grant agreement no. 801305), NanoHeatControl (POCI-01-0145-FEDER-031469), and HOTsPOT (POCI-01-0145-FEDER-031794), the last both funded by FEDER and Portuguese funds through FCT/MCTES, are acknowledged. RNS and AMPB thank NanoHeatControl for the grants.

References

[1] A.F.H. Goetz, Three decades of hyperspectral remote sensing of the earth: A personal view, Remote Sens. Environ. 113 (2009) S5-S16. https://doi.org/10.1016/j.rse.2007.12.014.

[2] Q.L. Li, X.F. He, Y.T. Wang, H.Y. Liu, D.R. Xu, F.M. Guo, Review of spectral imaging technology in biomedical engineering: Achievements and challenges, J. Biomed. Opt. 18 (2013) 100901. https://doi.org/10.1117/1.Jbo.18.10.100901.

[3] G.L. Lu, B.W. Fei, Medical hyperspectral imaging: A review, J. Biomed. Opt. 19 (2014) 010901. https://doi.org/10.1117/1.Jbo.19.1.010901.

[4] J.M. Amigo, Hyperspectral and multispectral imaging: Setting the scene, in: J.M. Amigo (Ed.) Data handling in science and technology, Elsevier, 2020, pp. 3-16.

[5] A. Iqbal, D.W. Sun, P. Allen, An overview on principle, techniques and application of hyperspectral imaging with special reference to ham quality evaluation and control, Food Control 46 (2014) 242-254. https://doi.org/10.1016/j.foodcont.2014.05.024.

[6] A.A. Gowen, C.P. O'Donnell, P.J. Cullen, G. Downey, J.M. Frias, Hyperspectral imaging - an emerging process analytical tool for food quality and safety control, Trends Food Sci. Tech. 18 (2007) 590-598. https://doi.org/10.1016/j.tifs.2007.06.001.

[7] N. Panov, D.S. Lu, E. Ortiz-Rivero, E.M. Rodrigues, P. Haro-Gonzalez, D. Jaque, E. Hemmer, Hyperspectral imaging and optical trapping: Complementary tools for assessing direction-dependent polarized emission from single upconverting liyf$_4$:Yb^{3+}/er^{3+} microparticles, Adv. Opt. Mater. 9 (2021) 2100101. https://doi.org/10.1002/adom.202100101.

[8] L. Giannoni, F. Lange, I. Tachtsidis, Hyperspectral imaging solutions for brain tissue metabolic and hemodynamic monitoring: Past, current and future developments, J. Opt. 20 (2018) 044009. https://doi.org/10.1088/2040-8986/aab3a6.

[9] N. Mehta, S. Shaik, R. Devireddy, M.R. Gartia, Single-cell analysis using hyperspectral imaging modalities, J. Biomech. Eng. 140 (2018) 0208021-02080216. https://doi.org/10.1115/1.4038638.

[10] P. Zamora-Perez, D. Tsoutsi, R.X. Xu, P. Rivera-Gil, Hyperspectral-enhanced dark field microscopy for single and collective nanoparticle characterization in biological environments, Materials 11 (2018) 243. https://doi.org/10.3390/ma11020243.

[11] G.A. Roth, S. Tahiliani, N.M. Neu-Baker, S.A. Brenner, Hyperspectral microscopy as an analytical tool for nanomaterials, Wiley Interdiscip. Rev.: Nanomed. Nanobiotechnology 7 (2015) 565-579. https://doi.org/10.1002/wnan.1330.

[12] M.E. Gosnell, A.G. Anwer, J.C. Cassano, C.M. Sue, E.M. Goldys, Functional hyperspectral imaging captures subtle details of cell metabolism in olfactory neurosphere cells, disease-specific models of neurodegenerative disorders, Biochim. Biophys. Acta, Mol. Cell Res. 1863 (2016) 56-63. https://doi.org/10.1016/j.bbamcr.2015.09.030.

[13] D.H. Lim, J. Jang, S. Kim, T. Kang, K. Lee, I.H. Choi, The effects of sub-lethal concentrations of silver nanoparticles on inflammatory and stress genes in human macrophages

using cdna microarray analysis, Biomaterials 33 (2012) 4690-4699. https://doi.org/10.1016/j.biomaterials.2012.03.006.

[14] M. Mortimer, A. Gogos, N. Bartolomé, A. Kahru, T.D. Bucheli, V.I. Slaveykova, Potential of hyperspectral imaging microscopy for semi-quantitative analysis of nanoparticle uptake by protozoa, Environ. Sci. Technol. 48 (2014) 8760-8767. https://doi.org/10.1021/es500898j.

[15] D. Yohan, C. Cruje, X.F. Lu, D. Chithrani, Elucidating the uptake and distribution of nanoparticles in solid tumors via a multilayered cell culture model, Nano-Micro Lett. 7 (2015) 127-137. https://doi.org/10.1007/s40820-014-0025-1.

[16] J.H. Shannahan, H. Sowrirajan, I. Persaud, R. Podila, J.M. Brown, Impact of silver and iron nanoparticle exposure on cholesterol uptake by macrophages, J. Nanomater. 2015 (2015) 127235. https://doi.org/10.1155/2015/127235.

[17] M.L. Debasu, C.D.S. Brites, S. Balabhadra, H. Oliveira, J. Rocha, L.D. Carlos, Nanoplatforms for plasmon-induced heating and thermometry, ChemNanoMat 2 (2016) 520-527. https://doi.org/10.1002/cnma.201600061.

[18] F. Akhatova, A. Danilushkina, G. Kuku, M. Saricam, M. Culha, R. Fakhrullin, Simultaneous intracellular detection of plasmonic and non-plasmonic nanoparticles using dark-field hyperspectral microscopy, Bull. Chem. Soc. Jpn. 91 (2018) 1640-1645. https://doi.org/10.1246/bcsj.20180198.

[19] A. Nadort, V.K.A. Sreenivasan, Z. Song, E.A. Grebenik, A.V. Nechaev, V.A. Semchishen, V.Y. Panchenko, A.V. Zvyagin, Quantitative imaging of single upconversion nanoparticles in biological tissue, Plos One 8 (2013) e63292. https://doi.org/10.1371/journal.pone.0063292.

[20] K. Kuruvinashetti, A.S. Kashani, S. Badilescu, D. Beaudet, A. Piekny, M. Packirisamy, Intracellular localized surface plasmonic sensing for subcellular diagnosis, Plasmonics 13 (2018) 1639-1648. https://doi.org/10.1007/s11468-017-0673-3.

[21] L.F. Leopold, D. Rugina, I. Oprea, Z. Diaconeasa, N. Leopold, M. Suciu, V. Coman, D.C. Vodnar, A. Pintea, C. Coman, Warfarin-capped gold nanoparticles: Synthesis, cytotoxicity, and cellular uptake, Molecules 24 (2019) 4145. https://doi.org/10.3390/molecules24224145.

[22] K. Darwiche, P. Zarogoulidis, L. Krauss, F. Oezkan, R.F.H. Walter, R. Werner, D. Theegarten, L. Sakkas, A. Sakkas, W. Hohenforst-Scmidt, K. Zarogoulidis, L. Freitag, "One-stop shop" spectral imaging for rapid on-site diagnosis of lung cancer: A future concept in nano-oncology, Int. J. Nanomed. 8 (2013) 4533-4542. https://doi.org/10.2147/Ijn.S54418.

[23] V. Mikulova, K. Kolostova, T. Zima, Methods for detection of circulating tumour cells and their clinical value in cancer patients, Folia Biol. (Praha) 57 (2011) 151-161.

[24] G.A. Sotiriou, F. Starsich, A. Dasargyri, M.C. Wurnig, F. Krumeich, A. Boss, J.C. Leroux, S.E. Pratsinis, Photothermal killing of cancer cells by the controlled plasmonic coupling of silica-coated au/fe_2o_3 nanoaggregates, Adv. Funct. Mater. 24 (2014) 2818-2827. https://doi.org/10.1002/adfm.201303416.

[25] S.Q. Zhu, K. Su, Y.M. Liu, H. Yin, Z. Li, F.R. Huang, Z.Q. Chen, W.D. Chen, G. Zhang, Y.H. Chen, Identification of cancerous gastric cells based on common features extracted from

hyperspectral microscopic images, Biomed. Opt. Express 6 (2015) 1135-1145. https://doi.org/10.1364/Boe.6.001135.

[26] P. Vallotton, B. Angel, M. Mccall, M. Osmond, J. Kirby, Imaging nanoparticle-algae interactions in three dimensions using cytoviva microscopy, J. Microsc. 257 (2015) 166-169. https://doi.org/10.1111/jmi.12199.

[27] S. Patskovsky, E. Bergeron, D. Rioux, M. Meunier, Wide-field hyperspectral 3d imaging of functionalized gold nanoparticles targeting cancer cells by reflected light microscopy, J. Biophotonics 8 (2015) 401-407. https://doi.org/10.1002/jbio.201400025.

[28] S.K. Chakkarapani, P. Zhang, S.H. Kang, 3d super-localization of intracellular organelle contacts at live single cell by dual-wavelength synchronized fluorescence-free imaging, Anal. Bioanal. Chem. 410 (2018) 1551-1560. https://doi.org/10.1007/s00216-017-0805-9.

[29] H. Shen, B. Xiong, R.L. Xu, X.D. Cheng, Y. He, E.S. Yeung, 3d darkfield imaging and single particle tracking of peptide-coated nanocargoes in live cells, Anal. Methods 6 (2014) 9202-9205. https://doi.org/10.1039/C4AY01813C.

[30] A.S. Luthman, S. Dumitru, I. Quiros-Gonzalez, J. Joseph, S.E. Bohndiek, Fluorescence hyperspectral imaging (fhsi) using a spectrally resolved detector array, J. Biophotonics 10 (2017) 840-853. https://doi.org/10.1002/jbio.201600304.

[31] S.L. Gai, P.P. Yang, D. Wang, C.X. Li, N. Niu, F. He, X.B. Li, Monodisperse gd_2o_3:Ln (ln = eu^{3+}, tb^{3+}, dy^{3+}, sm^{3+}, yb^{3+}/er^{3+}, yb^{3+}/tm^{3+}, and yb^{3+}/ho^{3+}) nanocrystals with tunable size and multicolor luminescent properties, CrystEngComm 13 (2011) 5480-5487. https://doi.org/10.1039/c1ce05455d.

[32] P.R. Twentyman, M. Luscombe, A study of some variables in a tetrazolium dye (mtt) based assay for cell-growth and chemosensitivity, Br. J. Cancer 56 (1987) 279-285. https://doi.org/10.1038/bjc.1987.190.

[33] F.J. Caixeta, A.R.N. Bastos, A.M.P. Botas, L.S. Rosa, V.S. Souza, A.N. Carneiro Neto, A. Ferrier, P. Goldner, L.D. Carlos, R.R. Gonçalves, R.A.S. Ferreira, High-quantum yield upconverting er^{3+}/yb^{3+} organic-inorganic hybrid dual coatings for real-time temperature sensing and photothermal conversion, J. Phys. Chem. C 124 (2020) 19892–19903. https://doi.org/10.1021/acs.jpcc.0c03874.

[34] C.D. Brites, X. Xie, M.L. Debasu, X. Qin, R. Chen, W. Huang, J. Rocha, X. Liu, L.D. Carlos, Instantaneous ballistic velocity of suspended brownian nanocrystals measured by upconversion nanothermometry, Nat. Nanotechnol. 11 (2016) 851-856. https://doi.org/10.1038/nnano.2016.111.

[35] C.D.S. Brites, A. Millán, L.D. Carlos, Lanthanides in luminescent thermometry, in: J.-C.G. Bünzli, V.K. Pecharsky (Eds.), Handbook on the physics and chemistry of rare earths, Elsevier Science, B. V., Amsterdam, 2016, pp. 339-427.

[36] C.D.S. Brites, P.P. Lima, N.J.O. Silva, A. Millán, V.S. Amaral, F. Palacio, L.D. Carlos, Thermometry at the nanoscale, Nanoscale 4 (2012) 4799-4829. https://doi.org/DOI: 10.1039/c2nr30663h.

[37] A. Paściak, A. Pilch-Wróbel, Ł. Marciniak, P.J. Schuck, A. Bednarkiewicz, Standardization of methodology of light-to-heat conversion efficiency determination for colloidal nanoheaters, ACS Appl. Mater. Interfaces 10.1021/acsami.1c12409 (2021). https://doi.org/10.1021/acsami.1c12409.

[38] R.V. Krishnan, G. Panneerselvam, P. Manikandan, M.P. Antony, K. Nagarajan, Heat capacity and thermal expansion of uranium-gadolinium mixed oxides, J. Nucl. Radiochem. Sci. 10 (2009) 19-26. https://doi.org/10.14494/jnrs.10.1_19.

[39] C.D.S. Brites, S. Balabhadra, L.D. Carlos, Lanthanide-based thermometers: At the cutting-edge of luminescence thermometry, Adv. Opt. Mater. 7 (2019) 1801239. https://doi.org/10.1002/adom.201801239.

[40] M. Suta, A. Meijerink, A theoretical framework for ratiometric single ion luminescent thermometers-thermodynamic and kinetic guidelines for optimized performance, Adv. Theor. Simul. 3 (2020) 2000176. https://doi.org/10.1002/adts.202000176.

[41] X.Y. Lv, X. Wang, T. Li, C.G. Wei, Y.A. Tang, T. Yang, Q.L. Wang, X.L. Yang, H.B. Chen, J.K. Shen, H. Yang, H.T. Ke, Rationally designed monodisperse gd_2o_3/bi_2s_3 hybrid nanodots for efficient cancer theranostics, Small 14 (2018) 1802904. https://doi.org/10.1002/smll.201802904.

[42] Y. Cheng, T. Lu, Y.D. Wang, Y.L. Song, S.Y. Wang, Q.L. Lu, L.F. Yang, F.P. Tan, J. Li, N. Li, Glutathione-mediated clearable nanoparticles based on ultrasmall gd_2o_3 for msot/ct/mr imaging guided photothermal/radio combination cancer therapy, Mol. Pharm. 16 (2019) 3489-3501. https://doi.org/10.1021/acs.molpharmaceut.9b00332.

[43] I.J. Standard, Biological evaluation of medical devices—part 5: Tests for in vitro cytotoxicity, in: S.I.O.f.S. Geneve (Ed.), 2009.

[44] M.L. Debasu, H. Oliveira, J. Rocha, L.D. Carlos, Colloidal $(gd_{0.98}nd_{0.02})_2o_3$ nanothermometers operating in a cell culture medium within the first and second biological windows, J. Rare Earths 38 (2020) 483-491. https://doi.org/10.1016/j.jre.2019.12.011.

[45] W. Gao, J. Dong, Z. Wang, Z. Zhang, H. Zheng, Multicolor upconversion emission of lanthanide-doped single $liyf_4$ and $liluf_4$ microcrystal, Mater. Res. Bull. 91 (2017) 77-84. https://doi.org/10.1016/j.materresbull.2017.03.043.

[46] F. Gonell, A.M.P. Botas, C.D.S. Brites, P. Amorós, L.D. Carlos, B. Julián-López, R.A.S. Ferreira, Aggregation-induced heterogeneities in the emission of upconverting nanoparticles at the submicron scale unfolded by hyperspectral microscopy, Nanoscale Adv. 1 (2019) 2537-2545. https://doi.org/10.1039/c8na00412a.

[47] S. Patskovsky, E. Bergeron, M. Meunier, Hyperspectral darkfield microscopy of pegylated gold nanoparticles targeting cd44-expressing cancer cells, J. Biophotonics 8 (2015) 162-167. https://doi.org/10.1002/jbio.201300165.

[48] P. Sarder, N. Arye, Deconvolution methods for 3-d microscopy images, IEEE Signal Process. Mag. 23 (2006) 32-45. https://doi.org/10.1109/MSP.2006.1628876.

[49] S. Balabhadra, M.L. Debasu, C.D.S. Brites, R.A.S. Ferreira, L.D. Carlos, Upconverting nanoparticles working as primary thermometers in different media, J. Phys. Chem. C 121 (2017) 13962-13968. https://doi.org/10.1021/acs.jpcc.7b04827.

[50] R. Piñol, C.D.S. Brites, R. Bustamante, A. Martínez, N.J.O. Silva, J.L. Murillo, R. Cases, J. Carrey, C. Estepa, C. Sosa, F. Palacio, L.D. Carlos, A. Millán, Joining time-resolved thermometry and magnetic-induced heating in a single nanoparticle unveils intriguing thermal properties, Acs Nano 9 (2015) 3134-3142. https://doi.org/DOI: 10.1021/acsnano.5b00059.

[51] R. Pinol, J. Zeler, C.D.S. Brites, Y.Y. Gu, P. Tellez, A.N.C. Neto, T.E. da Silva, R. Moreno-Loshuertos, P. Fernandez-Silva, A.I. Gallego, L. Martinez-Lostao, A. Martinez, L.D. Carlos, A. Millan, Real-time intracellular temperature imaging using lanthanide bearing polymeric micelles, Nano Lett. 20 (2020) 6466-6472. https://doi.org/10.1021/acs.nanolett.0c02163.

Figures

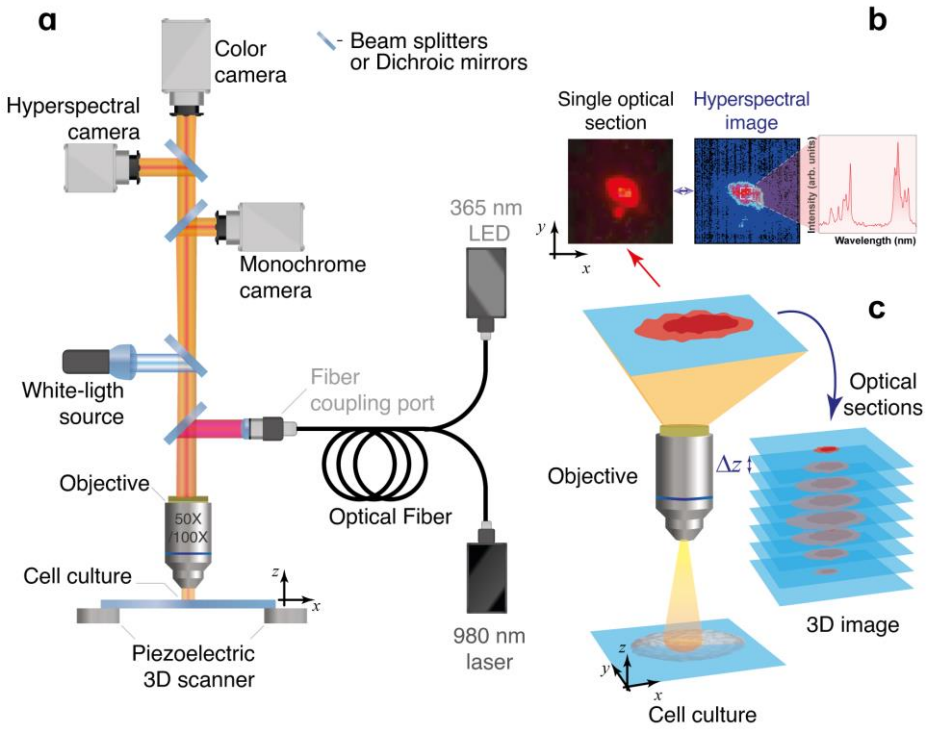

Figure 1. (a) Scheme of the used hyperspectral microscope. (b) Single optical section of the cell culture, recorded by the digital cameras and the corresponding hyperspectral image comprising one emission or scattering spectrum per pixel. (c) Construction of the 3D image by the composition of the optical sections acquired in distinct *z* planes, separated by Δz.

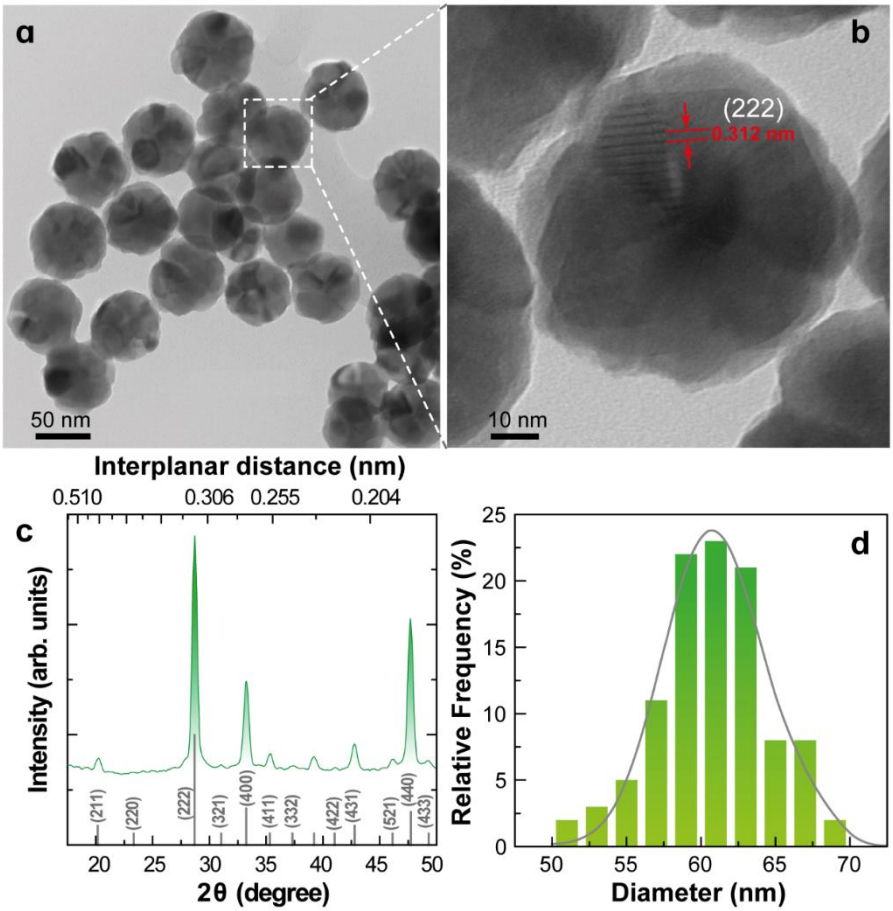

Figure 2. Representative TEM images of $(Gd_{0.97}Yb_{0.02}Er_{0.01})_2O_3$ at (a) low and (b) high magnification. In (b) the interplanar spacing between adjacent (222) planes of cubic Gd_2O_3 is depicted. (c) Powder XRD patterns of the nanoparticles showing reflections of the reference cubic Gd_2O_3 (PDF-4+ code: 04-003-4699). (d) Size distribution calculated from the TEM images using 100 representative nanoparticles. The solid line is the best fit to the experimental data using a log-normal distribution ($r^2 > 0.95$).

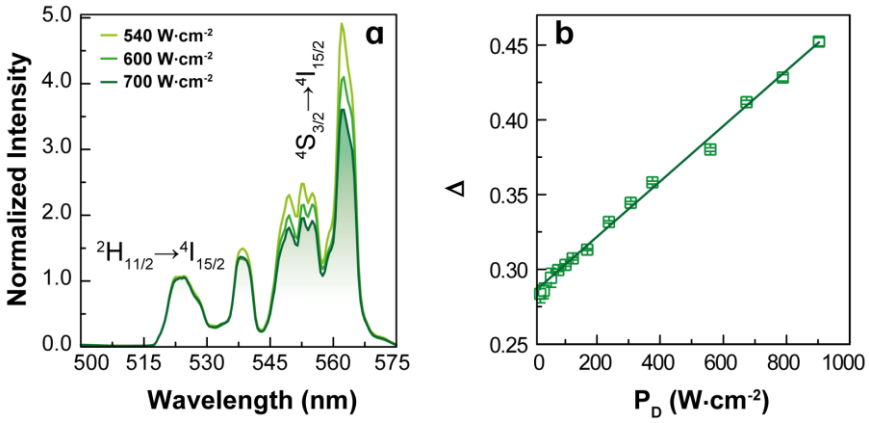

Figure 3. (a) Upconversion emission spectra of powdered $(Gd_{0.97}Yb_{0.02}Er_{0.01})_2O_3$ at room temperature under distinct 980 nm excitation power densities. (b) Dependence of the thermometric parameter with the laser power density.

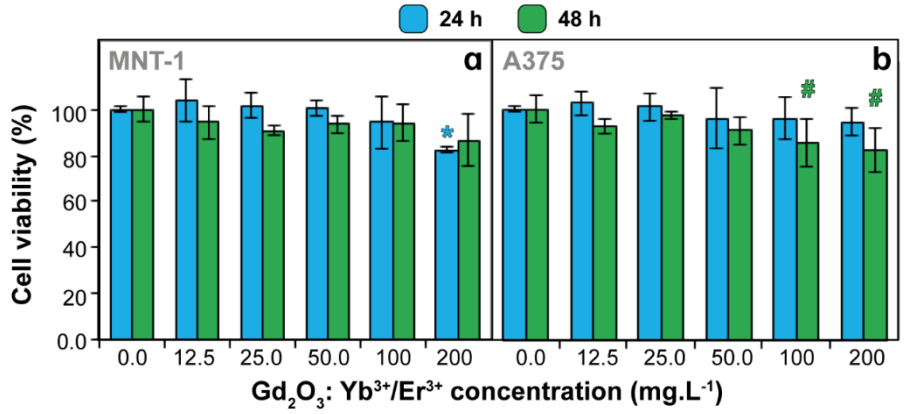

Figure 4. Cell viability of (a) MNT-1 and (b) A375 cell lines exposed to $(Gd_{0.97}Yb_{0.02}Er_{0.01})_2O_3$ nanoparticles for 24 and 48 h. Results are expressed as mean ± SD (standard deviation); the symbols * and # indicate a significant difference (p<0.05) between control, respectively at 24 and 48 h exposures.

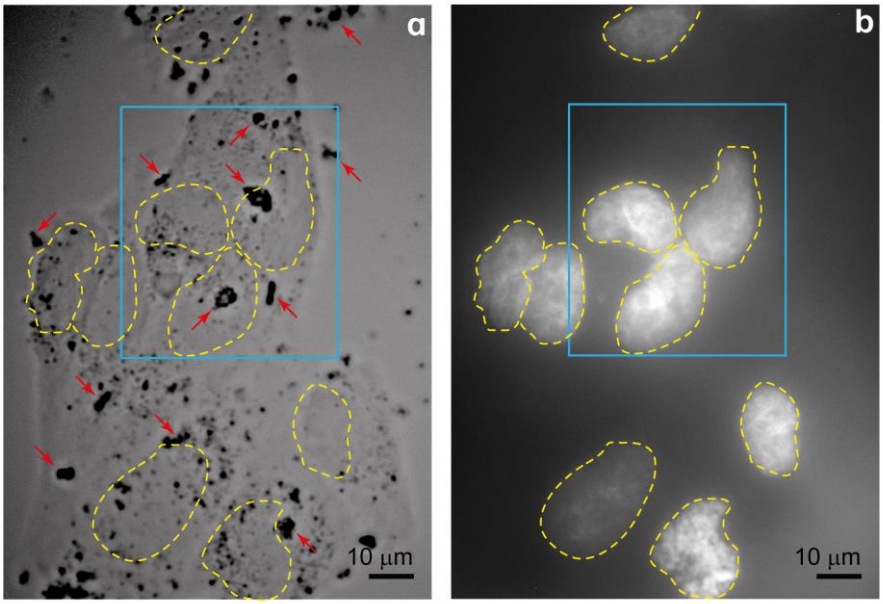

Figure 5. Bright-field optical images of DAPI-marked MNT-1 cells incubated with $(Gd_{0.97}Yb_{0.02}Er_{0.01})_2O_3$ nanoparticles in a fixed configuration acquired with the monochrome camera under (a) white-light illumination (transmission mode) and (b) UV irradiation (365 nm, reflection mode). The dashed lines delimitate the cell nucleus and the arrows mark nanoparticle clusters of different dimensions, visible as dark spots. The blue rectangle indicates the region analyzed in Figure 6.

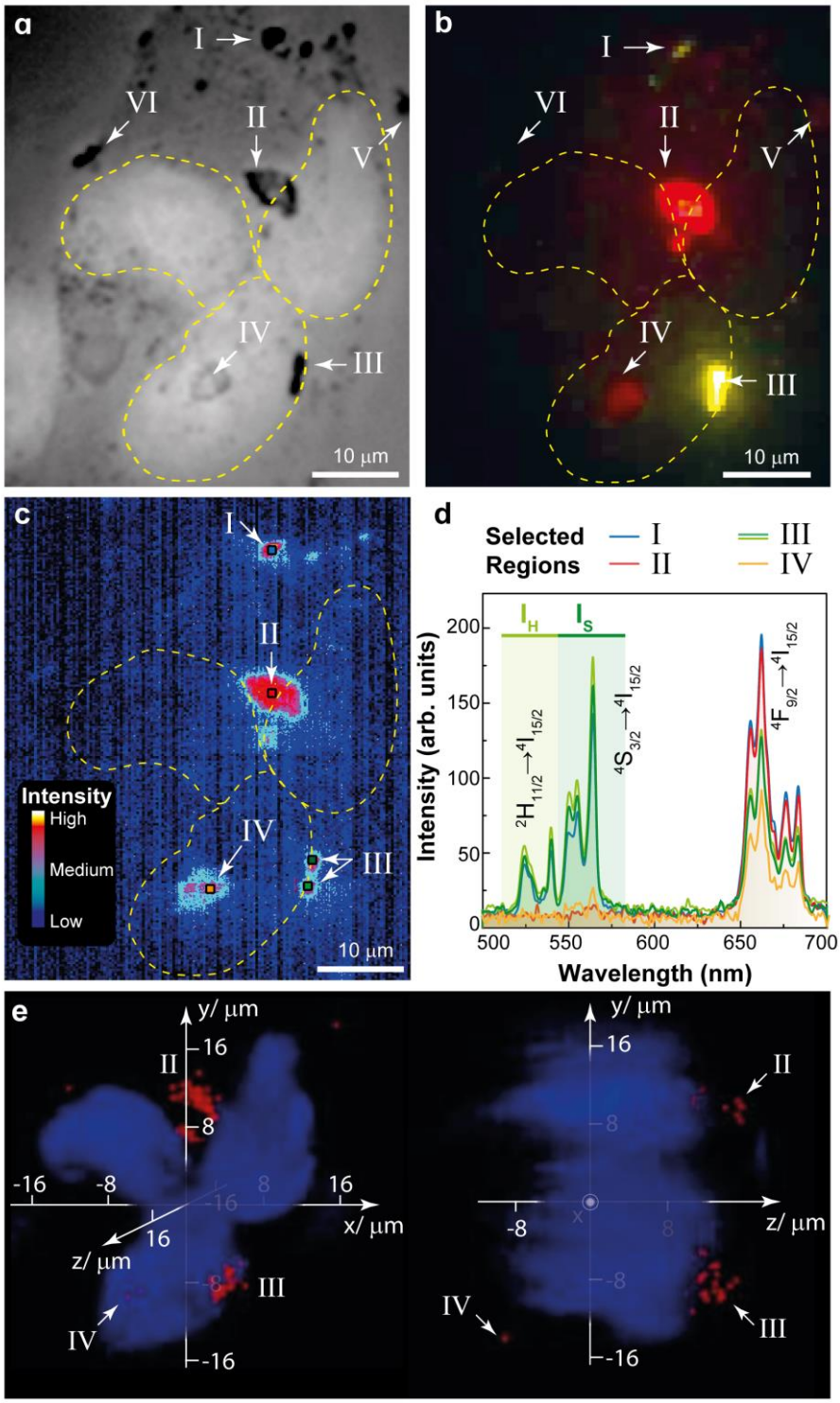

Figure 6. Bright-field 2D optical images of the region delimited by the blue rectangle in Figure 5 recorded at the $\boldsymbol{z = 0}$ plane under (a) white-light illumination (transmission mode, monochrome camera) and (b) 980 nm irradiation (reflection mode, color camera). (c) Hyperspectral image of the same region shown in (a) and (b). The color scale is based on the emission intensity at 662 nm (d) Emission spectra recorded in the selected regions (10×10 pixels^2) of the hyperspectral image shown in (c). (e) False-color 3D images showing the localization of the MNT-1 cancer cells nuclei (in blue) and $(Gd_{0.97}Yb_{0.02}Er_{0.01})_2O_3$ clusters in regions II, III, and IV (in red) within the cell culture volume.